


Efficient Electroabsorption Modulation of Mid- and Far-Infrared Radiation by Driving the Band-Inversion Transition of InAs/GaSb Type-II Quantum Wells

Jun Li^{1,*}, Jiang-Tao Liu^{2,†}, Zhenhua Wu³, Wei Huang¹, and Cheng Li¹

¹Department of Physics, Semiconductor Photonics Research Center, Xiamen University, Xiamen 361005, China

²College of Mechanical and Electrical Engineering, Guizhou Minzu University, Guiyang 550025, China

³Key Laboratory of Microelectronic Devices and Integrated Technology, Institute of Microelectronics, Chinese Academy of Sciences, Beijing, 100029, China

 (Received 6 May 2021; revised 25 October 2021; accepted 3 December 2021; published 22 December 2021)

Based on the self-consistent calculations of the eight-band $\mathbf{k} \cdot \mathbf{p}$ model and Poisson equation, we theoretically demonstrate that the intersubband optical absorption of InAs/GaSb type-II quantum wells (QWs) is effectively tuned by the electric-field-driven band-inversion transition. By utilizing this property, InAs/GaSb QWs can be made into highly efficient electroabsorption modulators (EAMs) for TM-polarized mid-infrared radiation (MIR) (approximately 4.2–12 μm) and TE-polarized far-infrared radiation (FIR) (approximately 12–100 μm). At low temperature, an example *p-i-n* waveguide EAM composed of six-period InAs/GaSb QWs achieves a drive voltage of < 0.5 V, a 3-dB cutoff bandwidth of approximately 24.6 GHz, and a dynamic power consumption of ≤ 0.06 mW/GHz for a 20-dB on:off ratio modulation of 4.46- μm TM-polarized radiation. Although the modulation efficiencies drop by 70%–80% when the temperature increases, the performance of InAs/GaSb EAMs is (at least) comparable with conventional 1.55- μm EAMs at 300 K. These results suggest that InAs/GaSb EAMs are promising devices for high-speed and low-power-consumption MIR (or FIR) free-space optical communications.

DOI: [10.1103/PhysRevApplied.16.064053](https://doi.org/10.1103/PhysRevApplied.16.064053)

I. INTRODUCTION

In past years, InAs/GaSb quantum wells (QWs) have attracted growing research attention in fundamental condensed-matter physics, since they act as versatile platforms for the investigations of many exotic quantum phenomena, such as, e.g., the quantum spin Hall effect [1,2], helical Luttinger liquids [3], the excitonic insulator phase [4–6], and anomalous magnetic oscillations [7,8]. The occurrence of these exotic phenomena benefits from the very distinctive feature of the InAs/GaSb heterostructure, i.e., the type-II (or broken-gap) band alignment that causes the two-dimensional (2D) electron and hole gases to coexist and distribute separately in InAs and GaSb layers, respectively. If the quantum confinement is not too strong, the InAs/GaSb QW will manifest an inverted band structure such that the ground conduction subband (E1) lies below the ground heavy-hole subband (HH1) at the Brillouin zone center, leading to the hybridization of electron and hole states, and opening a minigap at certain anti-crossing wave vectors [9,10]. This inverted band structure is topologically nontrivial for it protects a pair of gapless helical edge states and belongs to the 2D topological

insulator phase [1,2]. Additionally, from the perspective of applications, the family of InAs/GaSb/AlSb quantum structure systems have long been recognized as important infrared optoelectronic materials [11,12], and have been successfully used in fabricating the infrared photodetectors [13], quantum cascade lasers [14] (QCLs), and interband cascade lasers [14–16] (ICLs). Naturally, it would be promising to develop infrared optoelectronic devices based on InAs/GaSb QWs by taking advantage of their unique quantum features.

One other intriguing feature of InAs/GaSb type-II QWs is that their band structures can be switched between the normal band and inverted band, simply by varying the thickness of the InAs (GaSb) well and/or adjusting the external electric field [17–21]. Therefore, it is possible to manipulate the correlated physical properties of InAs/GaSb QWs by driving the band-inversion transition, e.g., by controlling the wells' thicknesses and/or sweeping the gate voltage. In this paper, we theoretically demonstrate that the intersubband optical absorption of InAs/GaSb type-II QWs can be effectively tuned by the applied gate bias, which gives rise to highly efficient electroabsorption (EA) modulations for TM-polarized mid-infrared radiation (TM-MIR) and TE-polarized far-infrared radiation (TE-FIR) (in the wavelength ranges of approximately 4.2–12 and 12–100 μm , respectively).

*lijun@xmu.edu.cn

†jtliau@semi.ac.cn

We propose that the electric-field-driven band inversion can be viewed as a special mechanism of EA modulation besides the conventional EA mechanisms, i.e., the Franz-Keldysh effect and quantum-confined Stark effect (QCSE) [22,23]. At low temperature, our calculations show that a typical *p-i-n* waveguide electroabsorption modulator (EAM) composed of six-period InAs/GaSb QWs is able to achieve a 20-dB on:off ratio modulation for TM MIR, with the drive voltage as low as < 0.5 V, a cutoff bandwidth of approximately 24.6 GHz, and an ultralow dynamic power consumption of ≤ 0.06 mW/GHz. Meanwhile, the TE FIR can also be modulated simultaneously, except for a smaller extinction ratio (about 1/3 that of TM MIR). At 300 K, although the modulation efficiencies degraded to a great extent, InAs/GaSb EAMs still manifest equal (or slightly better) performance compared to the commercialized 1.55- μm EAMs based on QCSE [22,23]. These results are interesting because they demonstrate the potential of InAs/GaSb EAMs for the application in high-speed free-space optical communications.

This paper is organized as follows. In Sec. II, we describe the theoretical model of InAs/GaSb QWs and present the calculated absorption spectra. In Sec. III, we discuss the motivation of developing high-speed EAMs in the MIR range and propose two possible configurations for the InAs/GaSb EAM. Then we assess the potential performance of InAs/GaSb *p-i-n* waveguide EAMs, and investigate the influence of temperature on the optical absorption and device operation. In Sec. IV we provide brief conclusions.

II. THEORY

A. Theoretical model of InAs/GaSb quantum wells under applied voltages

For the theoretical calculations, we consider that the InAs/GaSb QW is sandwiched between two symmetric AlSb barriers, with a total thickness of $d_w = d_{\text{InAs}} + d_{\text{GaSb}} + 2d_{\text{AlSb}}$, where d_{InAs} , d_{GaSb} , d_{AlSb} represent the thicknesses of the InAs, GaSb, AlSb layers, respectively. The electronic structures of InAs/GaSb type-II QWs under external gate bias can be calculated by a self-consistent model combining the eight-band $\mathbf{k} \cdot \mathbf{p}$ Hamiltonian and Poisson equation [10,24]

$$\{\hat{H}_0(\mathbf{k}) - e[V_{\text{in}}(z) + V_{\text{ex}}(z)]\}|\Psi_n(\mathbf{k})\rangle = E_n(\mathbf{k})|\Psi_n(\mathbf{k})\rangle, \quad (1a)$$

$$-\frac{d}{dz}\varepsilon_r(z)\frac{d}{dz}V_{\text{in}}(z) = -\rho_e(z) + \rho_h(z), \quad (1b)$$

$$-\frac{d}{dz}\varepsilon_r(z)\frac{d}{dz}V_{\text{ex}}(z) = 0. \quad (1c)$$

In the above equations, $\hat{H}_0(\mathbf{k})$ is the eight-band $\mathbf{k} \cdot \mathbf{p}$ Hamiltonian of the InAs/GaSb QW at zero field, and

$V_{\text{in(ex)}}(z)$ denotes the built-in (external) electric potential induced by the charge-redistribution effect (applied gate voltage). We can determine $V_{\text{ex}}(z)$ from the boundary conditions $-\int_0^{d_w}\varepsilon_r(z)(dV_{\text{ex}}/dz)dz = V_g^{\text{SP}}$ and $(dV_{\text{ex}}/dz)|_{z=0(d_w)} = 0$, where V_g^{SP} is the gate voltage applied on a single period of the InAs/GaSb QW (SP QW) and $\varepsilon_r(z)$ is the layer-dependent dielectric constant. The variables $E_n(\mathbf{k})$ and $|\Psi_n(\mathbf{k})\rangle$ are respectively the electron eigenenergy and eigenstate for an in-plane wave vector \mathbf{k} in the n th subband. The eigenstate $|\Psi_n(\mathbf{k})\rangle$ of the eight-band $\mathbf{k} \cdot \mathbf{p}$ Hamiltonian contains eight components of envelope functions, and can be expressed as $|\Psi_n(\mathbf{k})\rangle = \exp(i\mathbf{k} \cdot \boldsymbol{\rho})[\varphi_1^n(z), \varphi_2^n(z), \dots, \varphi_8^n(z)]^T$. Because the electron (hole) charge densities $\rho_{e(h)}(z)$ are dependent on the Fermi distribution function $f_n(E_F)$ and the envelope functions $\varphi_j^n(z)$, i.e.,

$$\rho_e(z) = \frac{e}{(2\pi)^2} \sum_n \int \sum_{j=1,2} |\varphi_j^n(z)|^2 f_n(E_F) d\mathbf{k}, \quad (2)$$

$$\rho_h(z) = \frac{e}{(2\pi)^2} \sum_n \int \sum_{j=3,4,\dots,8} |\varphi_j^n(z)|^2 [1 - f_n(E_F)] d\mathbf{k}, \quad (3)$$

Eqs. (1a) and (1b) are indeed coupled. Thus, a self-consistent iteration procedure is required to find the converged solutions. On each iteration step, the Fermi energy E_F is determined by the charge neutrality condition $\int_0^{d_w}[\rho_e(z) - \rho_h(z)]dz = 0$, while the Hamiltonian and Poisson equations are solved by the plane-wave expansion method [10,24,25]. The attained $E_n(\mathbf{k})$ and $|\Psi_n(\mathbf{k})\rangle$ can be used to calculate the absorption coefficients of InAs/GaSb QWs.

In Fig. 1, we display the calculated band diagrams, subband state probability densities, and band structures of a demonstrative SP QW under gate voltages of 0 and -0.7 V, which correspond to the normal and inverted band phases, respectively. Because the electron and hole states are spatially separated, the overlaps between their wave functions are relatively small, leading to substantially weak oscillator strengths for interband (i.e., valence-to-conduction band) optical absorption. However, for the intersubband transitions, such as the E1-E2, HH1-HH2 transitions, the oscillator strengths and optical absorption can be substantial. But the intersubband transitions are not allowed to happen until the E1 (HH1) subbands are populated with electrons (holes). By applying an adequate reverse gate voltage, such as $V_g^{\text{SP}} = -0.7$ V [in Figs. 1(b) and 1(d)], the orders of the E1 and HH1 subbands at $\mathbf{k} = 0$ could be inverted, accompanied with the electrons of HH1 (whose energies are higher than E_F) in GaSb transferring (or tunneling) to E1 in InAs, thus populating the E1 and HH1 subbands. Consequently, the intersubband transitions of E1-E2, HH1-HH2, and HH1 to other valence subbands

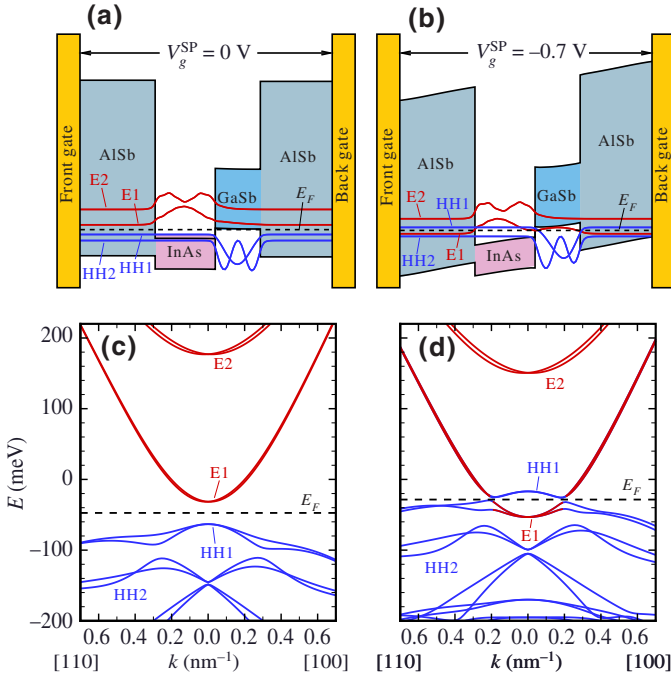


FIG. 1. Calculated band diagrams and probability densities of E2, E1, HH1 and HH2 eigenstates (at $\mathbf{k} = 0$) for a demonstrative InAs/GaSb QW at (a) $V_g^{\text{SP}} = 0$ V and (b) $V_g^{\text{SP}} = -0.7$ V. (c), (d) Band dispersions corresponding to (a) and (b), respectively. The red (blue) lines denote the probability densities [in (a) and (b)] or subband dispersions [in (c) and (d)] of electron (hole) states, respectively. In all panels, the black dashed lines mark the positions of Fermi energy levels. In this figure, the thicknesses of the InAs/GaSb/AISb layers are 8/6/10 nm.

(lower than HH2) can be turned on (or off) by applying proper gate voltages.

B. Single-particle optical absorption coefficients

For radiation linearly polarized along the μ th ($\mu = x, y, z$) direction, the absorption coefficient can be expressed as $\alpha^\mu(\omega) = 2\omega \text{Im}[\eta^\mu(\omega)]/c$, where ω is the light frequency, c is the speed of light in vacuum, and $\eta^\mu(\omega) = \sqrt{1 + \chi^\mu(\omega)}$ is the complex refractive index. In the framework of the single-particle approximation, the linear electric susceptibility is given by [26]

$$\chi^\mu(\omega) = \frac{\alpha_0 c}{\pi d_{\omega}} \sum_{mn} \int_{\text{BZ}} \frac{|v_{mn}^\mu|^2 f_{nm}(E_F)}{\omega_{mn}(\omega_{mn} - \omega - i\gamma)} d\mathbf{k}, \quad (4)$$

where $\omega_{mn} \equiv [E_m(\mathbf{k}) - E_n(\mathbf{k})]/\hbar$, $f_{nm}(E_F) \equiv f_n(E_F) - f_m(E_F)$, α_0 is the fine structure constant, $v_{mn}^\mu \equiv \langle \Psi_m(\mathbf{k}) | \hat{v}_\mu | \Psi_n(\mathbf{k}) \rangle$ is the matrix element of the velocity operator $\hat{v}_\mu = [\hat{r}, \hat{H}_0]/(i\hbar)$, and γ is the phenomenological damping parameter that relates to the scattering-induced depopulation and dephasing [27]. To numerically evaluate the Brillouin-zone integral in Eq. (4), we take γ to yield

a reasonable broadening of full width at half maximum (FWHM) ($2\hbar\gamma = 5$ meV) [28].

In real semiconductor samples, it is known that Coulomb many-body effects could make substantial contributions to the optical absorption [27]. To take full account of these effects, one needs to resort to sophisticated quantum many-body methods, such as the nonequilibrium Green functions [29] or density matrix formalism [30]. However, for narrow QWs with low or moderate carrier densities ($< 10^{16} \text{ m}^{-2}$), many-body effects were found to only cause minor peak shifts ($< 10\%$), and were dominated by the depolarization effect [27]. Therefore, in the main text we focus on the single-particle absorption coefficients, while the influence of the depolarization effect is briefly analyzed in Appendix A.

In the following, we consider two typical InAs/GaSb type-II QWs. The thicknesses of the InAs/GaSb/AISb layers for QW1 and QW2 are 5.5/8/5 and 12/5/5 nm, respectively. As displayed in Fig. 2, the optical absorption spectra of InAs/GaSb QWs in the inverted-band phase exhibit peaklike and strongly polarization-dependent behaviors, which just reflect the characteristics of the intersubband transition [27]. For TM polarization, several absorption peaks gradually show up in the mid-infrared radiation

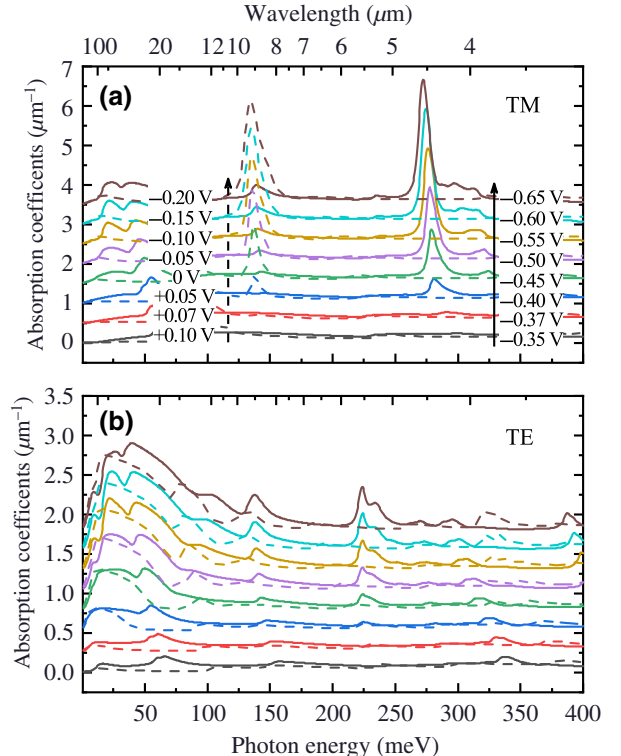


FIG. 2. Calculated absorption coefficient spectra of QW1 (solid lines) and QW2 (dashed lines) at low temperature for (a) TM and (b) TE polarization under different gate voltage biases. For QW1 (QW2), the gate voltage swing is from -0.35 ($+0.10$) to -0.65 (-0.20) V.

(MIR) range, elevating the reverse gate bias. Among them the most apparent ones are due to the E1-E2 transitions, i.e., the peaks around 278 (136) meV for QW1 (QW2), which are enabled and enhanced by the band-inversion-induced populating of E1 subbands. For QW1, one can find a secondary peak at approximately 140 meV in the TM absorption spectrum, which is ascribed to the HH1-LH1 transition (here LH1 denotes the top subband of GaSb light hole states), and it appears because of the mixing effect of the hole subbands. Note that we can observe slight red shifts of E1-E2 TM absorption peaks at high reverse voltages. This is because the anticrossing wave vectors \mathbf{k}_a move towards larger values for deeper band inversion. Meanwhile, at larger \mathbf{k}_a , the nonparabolic band dispersions cause smaller energy differences in the E1-E2 transitions, resulting in the red shifts of TM absorption peaks. It should be mentioned that if the many-body effects are taken into account, such red shifts could be (partly) compensated for by the depolarization shift (see Fig. 7 in Appendix A). On the other hand, the TE absorption peaks manifest broad and complex shapes, and locate mainly in the far-infrared radiation (FIR) range (approximately 12–100 μm), because they are contributed to by multi-inter-valence-subband transitions. But their magnitudes are only 30%–40% those of (E1-E2) TM absorption peaks. Interestingly, by varying the thickness of the InAs well (from 5 to 15 nm), the center of the TM absorption peak can be adjusted in the range of approximately 4.2–12 μm , covering most parts of the 3–5 and 8–13 μm MIR atmospheric transmission windows, thus implying that the EA modulations by InAs/GaSb type-II QWs might be very useful in high-speed MIR (or FIR) free-space optical communications [31–33].

III. ASSESSMENT OF InAs/GaSb ELECTROABSORPTION MODULATORS

A. Motivation towards high-speed mid-infrared modulators

Free-space optical communications (FSOCs) in the MIR range have gained renewed interest in recent years, owing to the progress of high-quality MIR sources, such as QCLs and ICLs [32–36]. Delga and Leviandier [32] envisioned that MIR FSOCs have the potential to be the most competitive communication technology in terms of all four dimensions, i.e., capacity, reach, cost, and availability [32]. However, to date, the development of MIR FSOCs is lagging behind other competing technologies, such as wireless radio-frequency and fiber-optic communication systems. To be commercially competitive, it is essential that MIR FSOCs achieve fast data-transfer rates (or wide bandwidths). As suggested by Delga and Leviandier, a good objective for future MIR FSOCs is to reach the modulation bandwidth of 40–50 GHz [32], which is the typical bandwidth of today’s fiber-optic communications. Obviously, MIR FSOCs with 40–50 GHz bandwidth would be

very attractive since they are at the fiber-optic speed but free of infrastructures.

QCLs have widely been considered as promising light sources for high-speed FSOCs, since QCLs were predicted to support ultrahigh direct-modulation frequencies (> 100 GHz), thanks to their short (picosecond scale) carrier lifetimes and the absence of relaxation oscillations [37]. Nevertheless, recent demonstrations of MIR-FSOC links with directly modulated QCLs only reached the maximum bandwidths of 1 GHz at room temperature [33–36]. Although there were other reports that specially designed QCLs could achieve direct modulation up to 26.5 GHz [38,39], they were measured under cryogenic temperatures, and some crucial metrics such as modulation depths and power efficiencies were also not given. It was then realized that the modulation frequencies of practical QCLs could be hindered by other factors, such as the parasitic circuits, lead inductances, and/or contact resistances [33–36]. Therefore, in practice, it is likely that high-speed external modulators could play indispensable roles for MIR FSOCs with bandwidths > 10 GHz, similarly to the roles 1.55- μm EAMs play in state-of-art fiber-optic systems. A recent experiment has just demonstrated the potential of external modulation devices by using a GaAs/(Al, Ga)As reflective modulator, which achieved a modulation frequency of 1.5 GHz for a 9.7- μm MIR beam at room temperature [40]. However, except for a few demonstrations [40–46], applicable MIR external modulators with desired high performance are currently underdeveloped [32,33,40]. In this sense, the electromodulation properties of InAs/GaSb QWs are very unique, as they shed light on developing high-performance MIR EAMs.

B. Possible configurations of InAs/GaSb electroabsorption modulators

Here, we present two possible device configurations of EAMs for the application of the InAs/GaSb QW’s electroabsorptive property: the *p-i-n* waveguide [Fig. 3(a)] and the vertical-incidence configuration [Fig. 3(b)].

The *p-i-n* waveguide diode is the most commonly used configuration for semiconductor EAMs. The waveguide of the EAM is very similar to that of a laser diode, so one can learn much about waveguide designing from type-II ICLs [15,47]. As shown in Fig. 3(a), for the InAs/GaSb EAM grown on an *n*-GaSb or *n*-GaAs substrate, one can firstly deposit a 0.5–1 μm *n*-doped GaSb layer as the buffer, and then the waveguide core can be disposed between the *n*⁺-doped (lower) and *p*⁺-doped (upper) InAs/AlSb short-period superlattice (SL) cladding layers [48]. The waveguide core is formed by sandwiching the multiperiod InAs/GaSb QWs between two *n*[−]-doped GaSb separate-confinement layers (SCLs). The two SCLs have high refractive indices that guarantee that the light intensity is confined in the waveguide core and effectively coupling

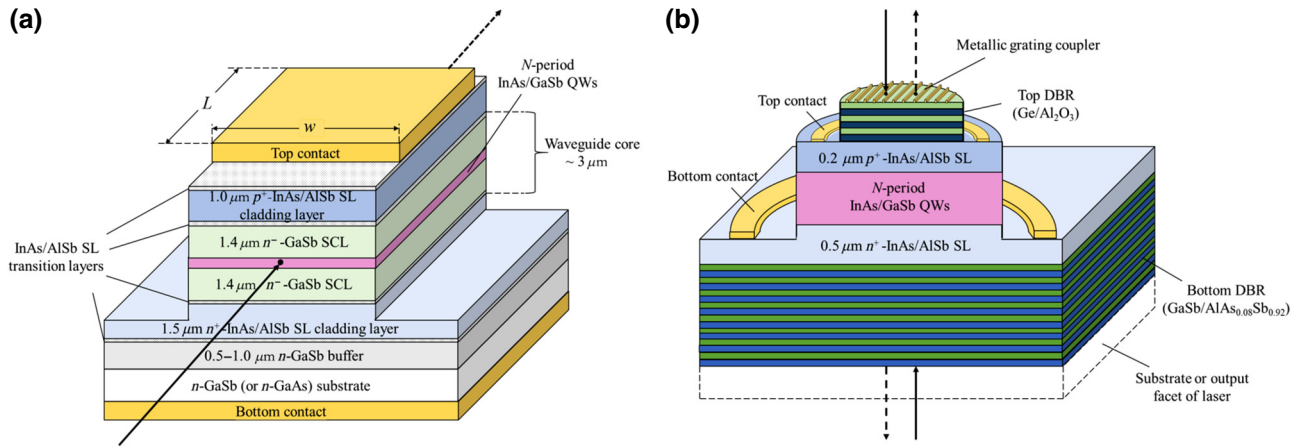


FIG. 3. Schematic plots of two possible configurations for InAs/GaSb EAMs: (a) device structure of the p - i - n waveguide diode configuration; (b) cross section of the vertical-incidence configuration.

with the InAs/GaSb QWs. The bottom and top contacts can be formed on the backside of the substrate and upper cladding layer, respectively. To reduce the parasitic voltages, one can introduce InAs/AlSb SLs as transition layers between the adjacent regions with abrupt band offset [15]. Besides, InAs/GaSb EAMs can also be prepared on an n -InAs substrate, just like the InAs-based ICLs [47]. But the InAs-based EAMs use [$n^+(p^+)$ -InAs]/[InAs/(Al, As)Sb SLs] as the plasmon cladding layers and n^- -InAs as the SCLs. After the material's growth, the device structure can be formed by photolithography and etching with the same technologies as those of the ICLs [15]. The thicknesses of each layer, the width w , and length L of the modulation region needs to be carefully designed to fulfill the desired performance of the EAM.

Another possible device structure for the InAs/GaSb EAM is the vertical-incidence configuration plotted in Fig. 3(b). Different from the p - i - n waveguide EAM, light is vertically incident on the plane of InAs/GaSb QWs, and parallel (or antiparallel) to the modulating electric field. This configuration can be constructed by inserting the multiperiod InAs/GaSb QWs (usually $N > 20$) between two heavily doped cladding layers (e.g., n^+ - and p^+ -InAs/AlSb SLs), while the top and bottom contacts are directly formed on the cladding layers, with transparent windows opening in the central regions of the contacts. Optionally, the vertical-incidence configuration of the EAM can incorporate an asymmetric Fabry-Pérot cavity [49] with different distributed Bragg reflectors (DBRs) at the bottom and top facets, so as to enhance the coupling of light with the InAs/GaSb QWs. The bottom and top DBRs can be fabricated similar to those in the interband cascade vertical-cavity surface-emitting laser (VCSEL) [50]. The disadvantage of the vertical-incidence configuration is that it cannot effectively couple the TM-polarized light; therefore, this configuration might be more useful for the modulation of TE FIR. For the modulation of TM MIR, it

would be necessary to introduce the metallic grating coupler [27] or the well-designed photonic crystal structure [51] on the top facet of the EAM to enhance coupling with the E1-E2 intersubband transition. Note that in this configuration both the top and bottom can be the input facet, and both the transmitted and reflected light can be modulated. The vertical-incidence EAM can either be grown on the substrate or directly integrated on top of the VCSEL, just as the GaAs/(Al, Ga)As EAM VCSEL [52]. One advantage of EAM VCSELs is that their fabrications do not rely on the regrowth process, which is currently unavailable for antimonide materials. But, instead, techniques for fabricating the double mesa structure and three contacts are required [53].

C. Performance of InAs/GaSb p - i - n waveguide electroabsorption modulators

Next, as an assessment for the prototype device, we study the potential performance of InAs/GaSb p - i - n waveguide EAMs, which is the most common configuration of semiconductor EAMs [22,54]. There are several figures of merit for a practical EAM to consider, such as the extinction ratio (ER), drive voltage, power consumption, modulation bandwidth, insertion loss, and device footprint [22,23,54]. The extinction (or on/off) ratio of a waveguide EAM is defined in decibels as [22]

$$10 \log \frac{T^\mu(V_{\text{on}})}{T^\mu(V_{\text{off}})} = T_{\text{dB}}^\mu(V_{\text{on}}) - T_{\text{dB}}^\mu(V_{\text{off}}), \quad (5)$$

where $T_{\text{dB}}^\mu(V) [\equiv 10 \log T^\mu(V)]$ is the radiation transmission as a function of the applied gate voltage in decibels, and $V_{\text{on(off)}}$ is the voltage of the high (low) transmittance state of the EAM. For μ -polarization radiation, the transmission function through an EA waveguide is expressed as

$$T^\mu(V) = K \exp[-\Gamma \alpha^\mu(V)L], \quad (6)$$

where K ($= 1$ for simplicity) is the coupling efficiency at the input and output of the waveguide and Γ is the optical confinement factor. For the EA waveguide embedded with SP QW, the optical confinement factor is estimated to be $\Gamma^{\text{SP}} \doteq 0.02$ according to Ref. [15]. For the EA waveguide embedded with multiperiod InAs/GaSb QWs (MP QWs), because Γ is approximately linear to the total thickness of MP QWs, d_w^{MP} (if $d_w^{\text{MP}} < 0.5 \mu\text{m}$) [15,23], it can be given by $\Gamma \approx N\Gamma^{\text{SP}}$, where N is the multiplicity of InAs/GaSb QWs. The drive voltage of the EAM is determined by the peak-to-peak swing of an on-off modulation, as $V_{\text{p.p.}} = |V_{\text{on}} - V_{\text{off}}|$. The dynamic drive power of the modulator can be evaluated by $P_{\text{ac}} = V_{\text{p.p.}}^2 / (8R)$, where R ($\approx 50 \Omega$) is the load resistor of the electric circuit [54]. The modulation bandwidth is given by the RC -limited 3-dB cutoff frequency, as $f_{3\text{-dB}} = 1 / (2\pi RC_j)$, where C_j is the capacitance of the p - i - n junction (where we have neglected the parasitic capacitance).

In Figs. 4(a) and 4(b), we exhibit the low-temperature transmission functions of two SP-QW EAMs for TM and TE polarization, respectively. According to Fig. 4 (a), one can choose V_{on} slightly below the critical voltage of band inversion, [e.g., setting $V_{\text{on}}^{\text{SP}} = -0.35$ (+0.10) V for QW1 (QW2)], so that an ER = 20 dB modulation of TM MIR can be driven by $V_{\text{p.p.}}^{\text{SP}} = 0.23$ (0.32) V for SP QW1 (SP QW2) at 4.52 (9.32) μm . These radiations with energies closest to the E1-E2 band-edge separations, i.e., with wavelengths of 4.46 and 9.12 μm , require the lowest drive voltages. But, increasing the reverse gate bias, transmissions for band-edge transitions saturate quickly and drop after. While, for radiations with longer wavelengths, transmissions may saturate at larger values and higher drive voltages, owing to the red shifts of the absorption peaks discussed previously (note that if one considers the compensation effect of the depolarization shifts to the red shifts, the saturation values and drive voltages for the band-edge transitions could be higher). For TE FIR [as shown in Fig. 4(b)], the extinction ratio (or modulation depth) is about 1/3 that of TM MIR at the same drive voltage, due to the smaller absorption coefficients. Our self-consistent calculations show that there are about $4.1 \times 10^{15} \text{ m}^{-2}$ carriers transferring through the InAs/GaSb interface during the 20-dB on-off operation of the EAM, which agrees well with the experiments in Ref. [20]. This carrier-transferring effect could induce a relatively large areal capacitance for SP QW, as $c_a^{\text{SP}} \approx 2.0$ – $4.1 \text{ fF}/\mu\text{m}^2$ at the *off* state, which constrains the modulation bandwidth (or speed) of SP-QW EAMs. One solution to this problem is to introduce MP QWs in the EA waveguide. Since the capacitance of MP QWs is the series connection of N SP-QW capacitors, i.e., $C_j^{\text{MP}} = c_a^{\text{SP}} wL / N$, where w and L are the width and length of the modulation region, respectively, InAs/GaSb EAMs with smaller capacitances (or higher bandwidths) can be obtained by increasing the QW's multiplicity N , at the cost of amplifying the drive

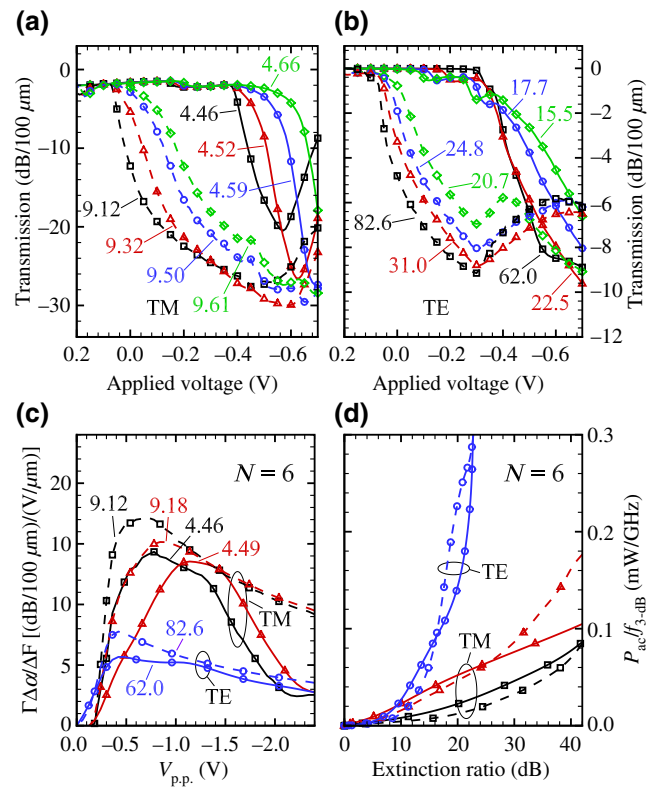


FIG. 4. Calculated transmission functions of two SP-QW EAMs (with $L = 100 \mu\text{m}$) for (a) TE and (b) TM polarization. Panels (c) and (d) show $\Gamma\Delta\alpha/\Delta F$ as a function of the drive voltage and $P_{\text{ac}}/f_{3\text{-dB}}$ as a function of the extinction ratio, respectively, for six-period QW EAMs with $w = 5 \mu\text{m}$ and $L = 50 \mu\text{m}$. In all panels, the solid (dashed) lines represent the results for QW1 (QW2) at different wavelengths (measured in micrometers). All calculations in this figure are done at low temperature.

voltage N times for the same band-inversion status, accompanied by an enlarged extinction ratio and insertion loss (i.e., the residue absorption at the *on* state).

As an example, here we consider an EAM made of six-period InAs/GaSb QWs (6P QWs) with $w = 5 \mu\text{m}$ and $L = 50 \mu\text{m}$. The bandwidth of this EAM is found to be approximately 24.6 GHz, and the drive voltage is approximately 0.48 V for ER = 20 dB of the 4.46- μm TM MIR, which produces a high bandwidth-to-drive-voltage ratio of 51.25 GHz/V (about 1.5–2 times that reported for 1.55- μm EAMs [55,56]). In Figs. 4(c) and 4(d), we calculate the modulation-depth-to-electric-field ratio $\Gamma\Delta\alpha/\Delta F$ [22] and drive-power-to-bandwidth ratio $P_{\text{ac}}/f_{3\text{-dB}}$ [54] for two 6P-QW EAMs, which measure the modulation and dynamic power consumption efficiency, respectively. It can be seen that the maximum of $\Gamma\Delta\alpha/\Delta F$ reaches 13–17 (dB/100 μm)/(V/ μm) for TM MIR (about 4 to 6 times that reported for 1.55- μm EAMs [57]). At low temperature, $P_{\text{ac}}/f_{3\text{-dB}}$ for ER = 20 dB is found to be 0.02–0.06 mW/GHz for TM MIR and 0.15–0.21 mW/GHz

for TE FIR, which are even lower than the predicted theoretical limits (approximately 0.22 mW/GHz) [58] of EAMs based on QCSE.

In addition, shortening the length L or increasing the total thickness d_w could offer other approaches to reducing the capacitances of InAs/GaSb waveguide EAMs. Since including too many periods of InAs/GaSb QWs will also enlarge the insertion loss, and the length of EAM cannot be too-short for cleaving, one might consider increase d_w by expanding the thickness of AlSb barrier, i.e., d_{AlSb} , to reduce the capacitance of QW. For example, if one increases d_{AlSb} by Δd_{AlSb} then the capacitance can be approximately reduced from C_j to $[d_w/(d_w + 2\Delta d_{\text{AlSb}})]C_j$, while the drive voltage is lifted from $V_{\text{p.p.}}$ to $(1 + 2\Delta d_{\text{AlSb}}/d_w)V_{\text{p.p.}}$. Hence, there is a simple trade-off between the capacitance (or modulation bandwidth) and the drive voltage through controlling d_{AlSb} . Since the bandwidth-to-drive-voltage ratio of InAs/GaSb EAMs could be as high as 51.25 GHz/V at low temperature (even higher than the conventional semiconductor EAMs based on QCSE), there is plenty of room to optimize the trade-offs among the extinction ratio, drive voltage, and modulation bandwidth, thus making it possible for InAs/GaSb EAMs to achieve the desired modulation frequency and power consumption.

D. Influence of temperature

Because of the narrow-gap nature of InAs/GaSb QWs, their absorption spectra can be greatly altered by the temperature effect. In Fig. 5, we display the TM-polarized absorption coefficients of QW1 at different temperatures and under the on-off voltages. It can be seen that, by raising the temperature, the intersubband absorption peaks for the E1-E2 transition gradually show up for -0.35 V (*on* state), but would be weakened and broadened for -0.7 V (*off* state). This is due to the thermal excitations significantly changing the carrier population distributions in their subbands, thus greatly affecting the intersubband transitions (see the detailed illustration in Appendix B). The changes in absorption impair the extinction ratio and also increase the insertion loss of InAs/GaSb EAMs. Therefore, to maintain the required extinction ratio and keep the insertion low, one usually needs to set a higher voltage for the *off* state and a lower (or even reversed) voltage for the *on* state. As a result, the modulation efficiencies of InAs/GaSb EAMs degrades with increasing temperature.

In Fig. 6(a), we show the influence of temperature on the transmission functions of a 6P-QW EAM. It can be seen that the absolute slopes of the transmission functions generally decrease with increasing temperature, indicating that the modulation efficiencies decline as well. From 4 to 300 K, $\Gamma \Delta\alpha/\Delta F$ is found to drop by about 70%–80%. But, fortunately, at 300 K, it still holds a value of approximately 3.2 (dB/100 μm)/(V/ μm) for ER = 20 dB of 4.46- μm

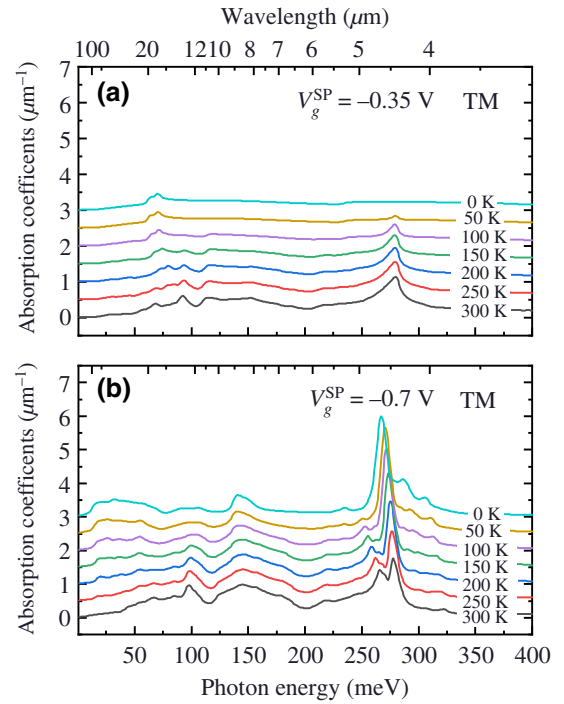


FIG. 5. Calculated absorption coefficient spectra of QW1 at different temperatures for TM polarization under (a) -0.35 V (*on* state) and (b) -0.7 V (*off* state).

TM MIR, which is comparable to (or slightly better than) the conventional 1.55- μm EAM based on QCSE [57]. In Fig. 6(b), we plot $P_{\text{ac}}/f_{3\text{-dB}}$ as a function of temperature. From this figure, we see that $P_{\text{ac}}/f_{3\text{-dB}}$ increases about 0.3 (0.43) mW/GHz for ER = 20 (15) dB of TM MIR (TE FIR) when the temperature is increased from 4 to 300 K.

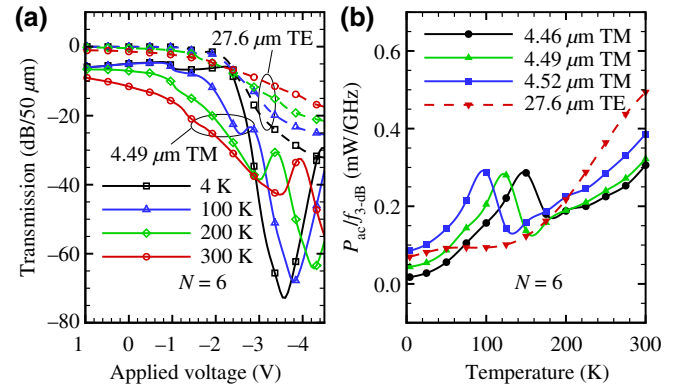


FIG. 6. (a) Transmission functions of a typical InAs/GaSb EAM at different temperatures for TM (solid lines) and TE (dashed lines) polarization. The lines with hollow squares, triangles, diamonds, and circles respectively denote the data taken at 4, 100, 200, and 300 K. (b) Drive-power-to-bandwidth ratio as a function of temperature for TM-MIR (TE-FIR) modulation of ER = 20 (15) dB. In this figure, the modulator is assumed to comprise six periods of QW1, with $w = 5$ μm and $L = 50$ μm .

The oscillations of the curves seen in Figs. 6(a) and 6(b) are due to the absorption-peak-red-shift-induced interplay of the neighboring intersubband transitions.

Lastly, we should mention that the above performance of InAs/GaSb *p-i-n* waveguide EAMs is estimated in a rough but conservative way. For example, we have assumed a general 50 Ω load resistor for the estimation of the cut-off bandwidth. In practice, the device resistance could be much lower, since nowadays InAs/GaSb QW samples with very high mobility are available [59], which could directly give the reward of a higher bandwidth. In addition, the optical confinement factor Γ , the width w and length L of the modulation region can still be optimized by performing full optical fields and device simulations. Therefore, one can further improve the performance (especially at room temperature) of InAs/GaSb EAMs using high-quality samples, carefully compromising the structure of the waveguide, the multiplicity of QWs, and the thicknesses of the InAs/GaSb/AlSb layers, as well as engineering the band structures of type-II QWs with strain and $\text{Ga}_x\text{In}_{1-x}\text{Sb}$ alloys [60,61].

IV. CONCLUSIONS

In summary, we have demonstrated that electric-field-driven band-inversion of the InAs/GaSb QW can support the EA modulation of MIR and FIR at ultrahigh efficiencies. At low temperature, the performance of typical *p-i-n* waveguide InAs/GaSb EAMs is notably superior to that of conventional 1.55- μm EAMs based on QCSE. Because of the temperature sensitiveness of narrow-gap semiconductor devices, the modulation efficiencies of InAs/GaSb EAMs degrade with increasing temperature, but remains comparable with conventional EAMs at 300 K. In addition, InAs/GaSb EAMs typically have a small device footprint, and are compatible with antimonide materials, which facilitate their monolithic integration with antimonide-based MIR (of FIR) sources [62,63]. Therefore, InAs/GaSb EAMs provide vast potential for developing high-speed and low-power-consumption MIR (or FIR) free-space optical communications.

ACKNOWLEDGMENTS

J.L. is mainly supported by the Natural Science Foundation of Fujian Province of China (Grant No. 2020J01008) and partly supported by the NSFC (Grant No. 11675133). J.-T.L. is supported by the 13th batch of Outstanding Young Scientific and Technological Talents Project in Guizhou Province (No. [2021]5618). Z.W. is supported by the Academy of Integrated Circuit Innovation under Grant No. Y8YC01X001.

APPENDIX A: INFLUENCE OF THE DEPOLARIZATION EFFECT

The many-body effects, including the depolarization effect, the exchange-correlation induced self-energy, and excitonic (or vertex) corrections, are known to have non-negligible impacts on the intersubband absorption spectra of QWs with high free-electron densities [29,64]. Among these many-body effects, the depolarization effect was found to be the dominant one in most cases [27]. To incorporate the depolarization effect, we extend the two-level model of modified conductivity (with depolarization shift) $\tilde{\sigma}_{zz}(\omega)$ in Refs. [27,64–66], and rewrite the modified two-level linear susceptibility as

$$\tilde{\chi}_{mn}^z(\omega) = \frac{\chi_{mn}^z(\omega)}{1 + (\bar{a} - \bar{b})G(\omega)}, \quad (\text{A1})$$

where we have used the relation $\sigma_{zz}(\omega) = -i\omega\varepsilon_0\chi_{mn}^z(\omega)$. In the above equations, $\sigma_{zz}(\omega)$ and $\chi_{mn}^z(\omega)$ are the single-particle two-level conductivity and linear susceptibility for radiation linearly polarized along the z direction, respectively; the total single-particle linear susceptibility is given by $\chi^z(\omega) = \sum_{mn} \chi_{mn}^z(\omega)$; \bar{a} and \bar{b} characterize the depolarization shift and excitonic correction shift, respectively. It has been shown that \bar{b} is usually much smaller than \bar{a} [27], so we can simply neglect \bar{b} here (i.e., the excitonic correction). For the E1-E2 intersubband transition (below we label $1 \rightarrow \text{E1}$, $2 \rightarrow \text{E2}$ for short), the expression for

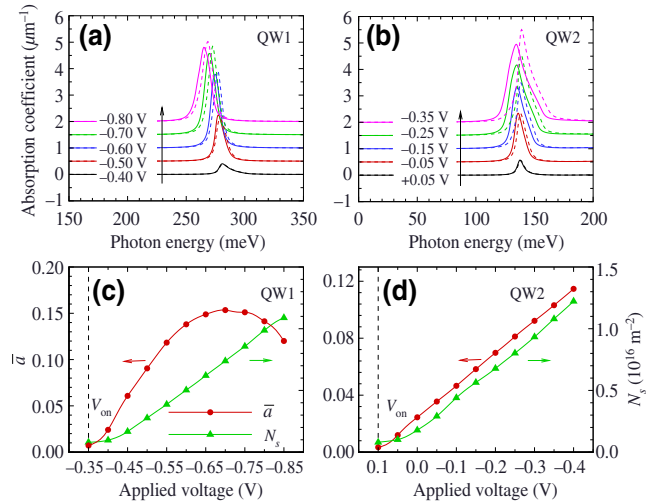


FIG. 7. The calculated two-level absorption coefficients of the E1-E2 transition at different gate voltages for (a) QW1 and (b) QW2. The solid (dashed) lines denote the intersubband absorption with (without) depolarization effect. (c),(d) Self-consistent calculation results of \bar{a} and N_s as functions of the applied voltages for QW1 and QW2, respectively. The dashed lines mark the voltages that are set for V_{on} . All curves are for TM-polarized radiations.

\bar{a} is

$$\bar{a} = \frac{g_s}{N_s(2\pi)^2} \int f_{12}(E_F) a_{12}(\mathbf{k}) d\mathbf{k} \quad (\text{A2})$$

$$S(\mathbf{k}) = \int_0^{d_w} \left(\int_0^z \langle z' | \Psi_2(\mathbf{k}) \rangle \langle \Psi_1(\mathbf{k}) | z' \rangle dz' \right)^2 dz. \quad (\text{A3})$$

The function $G(\omega)$ is given by

$$\text{with } f_{12}(E_F) \equiv f_1(E_F) - f_2(E_F), \quad a_{12}(\mathbf{k}) = 2e^2 N_s S(\mathbf{k}) / [\varepsilon_r \hbar \omega_{21}(\mathbf{k})], \text{ and} \quad G(\omega) = \frac{g_s}{N_s(2\pi)^2} \int \frac{f_{12}(E_F) \omega_{21}^2(0)}{\omega_{21}^2(\mathbf{k}) - \omega^2 - 2i\omega\gamma} d\mathbf{k}, \quad (\text{A4})$$

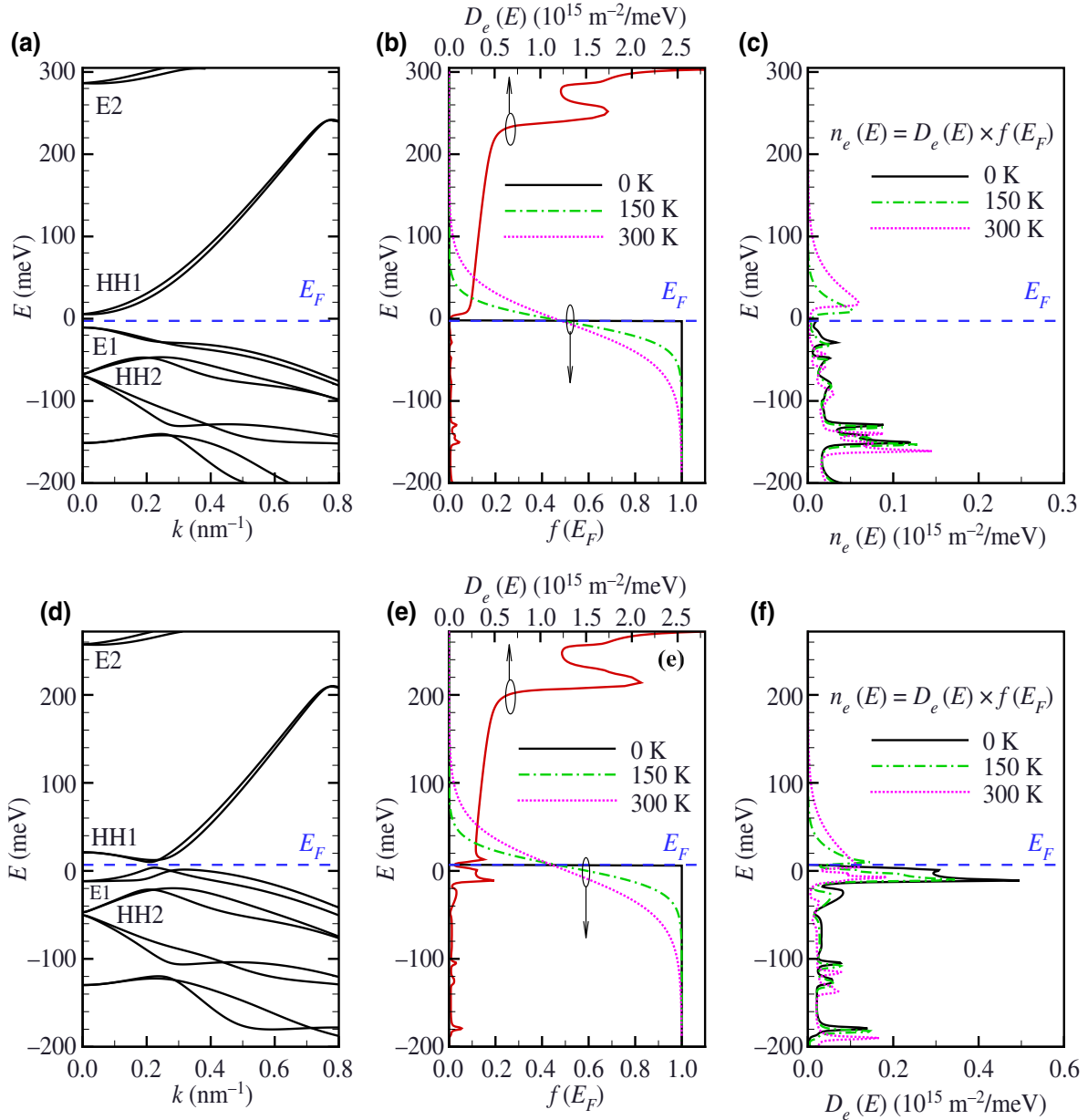


FIG. 8. (a) Band structures; (b) electron densities of states and Fermi distribution functions; (c) electron population as a function of energy at different temperatures for 5.5/8/5 (nm) the single-period InAs/GaSb QW under -0.35 V (on state). Panels (d)–(f) are similar to (a)–(c), but for the single-period InAs/GaSb QW under -0.7 V (off state). The red solid lines in (b) and (e) are the electron densities of states that appear in the InAs layer. The black solid, dashed blue, dotted purple lines in (b) and (d) denote the Fermi distribution functions for 0, 150, and 300 K, respectively. Those lines in (c) and (f) correspond to the electron populations at different temperatures.

where g_s is the spin degeneracy and N_s is the free-electron density (due to band-inversion-induced charge transferring). The renormalized resonance frequency is given by $\tilde{\omega}_{21}^2 = \omega_{21}^2(1 + \bar{a} - \bar{b})$. Accordingly, the relative depolarization shift can be simply estimated by $(\tilde{\omega}_{21} - \omega_{21})/\omega_{21} \approx 0.5\bar{a}$.

It can be seen from Figs. 7(a) and 7(b) that the depolarization would cause blue shifts and sharper peaks for the intersubband absorption of TM-polarized radiation. The depolarization shift in InAs/GaSb QWs will increase with the transferred electron density (or drive voltage), or be larger in the wider electron well, e.g., in QW2 (than in QW1). These results are consistent with the predictions in Ref. [27], that is, the depolarization effect will be more notable for QWs with higher free-electron densities or smaller subband-subband energy separations. As demonstrated in Figs. 7(c) and 7(d), for moderate SP-QW drive voltages $V_{p.p.}^{SP} (= |V_{on}^{SP} - V_{off}^{SP}|) < 0.5$ V, the transferred electron densities are generally less than $1.3 \times 10^{16} \text{ m}^{-2}$, which limits the relative depolarization shifts ($0.5\bar{a}$) to be smaller than 0.8% and 6% for QW1 and QW2, respectively. Note that the calculated \bar{a} for QW1 [see Fig. 7(c)] could saturate with increasing applied voltage; this is because at large anticrossing wave vectors (or maximal transition wave vector) \mathbf{k}_a , the states of the E2 subband are getting close to the height of the barrier, thus suppressing the change of overlap between $|\Psi_1(\mathbf{k})\rangle$ and $|\Psi_2(\mathbf{k})\rangle$. Meanwhile, by increasing the applied voltage, the depolarization shift will compete with the nonparabolic dispersion-induced red shift, leading to a higher modulation extinction ratio (or modulation depth) and saturated drive voltage for an InAs/GaSb EAM at the resonance wavelength. These corrections are actually positive to the performance of the EAM. But, in general, within the on-off voltage swing, the depolarization only has a minor impact on the modulation of TM MIR, and has no influence on that of TE FIR. Therefore, the inclusion of the depolarization effect would not qualitatively change our conclusions in the main text.

APPENDIX B: ILLUSTRATION OF PERFORMANCE DEGRADATION WITH INCREASING TEMPERATURE

To further illustrate the influence of temperature on the intersubband absorption of InAs/GaSb QWs, in Fig. 8 we exhibit the band structures [in (a) and (d)] and the corresponding electron densities of states $D_e(E)$ [in (b) and (e)] for the example InAs/GaSb QW under the *on* and *off* states, respectively. The influence of temperature is attributed to changes in Fermi distribution functions, i.e., $f(E_F)$ as plotted in panels (b) and (d), which lead to variations in the occupied electron populations, i.e., given by $n_e(E) = D_e(E)f(E_F)$ in panels (c) and (f). It can be seen that, for the *on* state, increasing the temperature causes

partial occupation of the E1 subband by thermally excited electrons, thus enabling the E1-E2 intersubband transition. For the *off* state, the occupied electron population spreads to a wider energy range by temperature-induced $f(E_F)$ changes, which weaken and broaden the absorption peaks. The changes in absorption for both the *on* and *off* states are responsible for the performance degradation of InAs/GaSb EAMs.

-
- [1] C. Liu, T. L. Hughes, X.-L. Qi, K. Wang, and S.-C. Zhang, Quantum Spin Hall Effect in Inverted Type-II Semiconductors, *Phys. Rev. Lett.* **100**, 236601 (2008).
 - [2] I. Knez, R.-R. Du, and G. Sullivan, Evidence for Helical Edge Modes in Inverted InAs/GaSb Quantum Wells, *Phys. Rev. Lett.* **107**, 136603 (2011).
 - [3] T. Li, P. Wang, H. Fu, L. Du, K. A. Schreiber, X. Mu, X. Liu, G. Sullivan, G. A. Cs athy, X. Lin, and R.-R. Du, Observation of a Helical Luttinger Liquid in InAs/gaSb Quantum Spin Hall Edges, *Phys. Rev. Lett.* **115**, 136804 (2015).
 - [4] L. Du, X. Li, W. Lou, G. Sullivan, K. Chang, J. Kono, and R.-r. Du, Evidence for a topological excitonic insulator in InAs/GaSb bilayers, *Nat. Commun.* **8**, 1971 (2017).
 - [5] W. Yu, V. Cleric , C. H. Fuentevilla, X. Shi, Y. Jiang, D. Saha, W. K. Lou, K. Chang, D. H. Huang, G. Gumbs, D. Smirnov, C. J. Stanton, Z. Jiang, V. Bellani, Y. Meziani, E. Diez, W. Pan, S. D. Hawkins, and J. F. Klem, Evidence for an excitonic insulator phase in a zero-gap InAs/GaSb bilayer, [arXiv:1701.07417](https://arxiv.org/abs/1701.07417), 1 (2017).
 - [6] X.-J. Wu, W. Lou, K. Chang, G. Sullivan, A. Ikhlassi, and R.-R. Du, Electrically tuning many-body states in a Coulomb-coupled InAs/InGaSb double layer, *Phys. Rev. B* **100**, 165309 (2019).
 - [7] D. Xiao, C.-X. Liu, N. Samarth, and L.-H. Hu, Anomalous Quantum Oscillations of Interacting Electron-Hole Gases in Inverted Type-II InAs/GaSb Quantum Wells, *Phys. Rev. Lett.* **122**, 186802 (2019), [arXiv:1812.05238](https://arxiv.org/abs/1812.05238).
 - [8] Z. Han, T. Li, L. Zhang, G. Sullivan, and R.-R. Du, Anomalous Conductance Oscillations in the Hybridization Gap of InAs/GaSb Quantum Wells, *Phys. Rev. Lett.* **123**, 126803 (2019).
 - [9] M. J. Yang, C. H. Yang, B. R. Bennett, and B. V. Shanabrook, Evidence of a Hybridization Gap in ‘‘Semimetallic’’ InAs/GaSb Systems, *Phys. Rev. Lett.* **78**, 4613 (1997).
 - [10] J. Li, W. Yang, and K. Chang, Spin states in InAs/AlSb/GaSb semiconductor quantum wells, *Phys. Rev. B* **80**, 035303 (2009).
 - [11] H. Kroemer, The family (InAs, GaSb, AlSb) and its heterostructures: A selective review, *Phys. E: Low-Dimens. Syst. Nanostructures* **20**, 196 (2004).
 - [12] P. S. Dutta, H. L. Bhat, and V. Kumar, The physics and technology of gallium antimonide: An emerging optoelectronic material, *J. Appl. Phys.* **81**, 5821 (1997).
 - [13] A. Rogalski, P. Martyniuk, and M. Kopytko, InAs/GaSb type-II superlattice infrared detectors: Future prospect, *Appl. Phys. Rev.* **4**, 031304 (2017).

- [14] A. N. Baranov and R. Teissier, Quantum cascade lasers in the InAs/AlSb material system, *IEEE J. Sel. Top. Quantum Electron.* **21**, 85 (2015).
- [15] I. Vurgaftman, R. Weih, M. Kamp, J. R. Meyer, C. L. Canedy, C. S. Kim, M. Kim, W. W. Bewley, C. D. Merritt, J. Abell, and S. Höfling, Interband cascade lasers, *J. Phys. D: Appl. Phys.* **48**, 123001 (2015).
- [16] J. Meyer, W. Bewley, C. Canedy, C. Kim, M. Kim, C. Merritt, and I. Vurgaftman, The interband cascade laser, *Photonics* **7**, 75 (2020).
- [17] Y. Naveh and B. Laikhtman, Band-structure tailoring by electric field in a weakly coupled electron-hole system, *Appl. Phys. Lett.* **66**, 1980 (1995).
- [18] M. Drndic, M. P. Grimshaw, L. J. Cooper, D. A. Ritchie, and N. K. Patel, Tunable electron-hole gases in gated InAs/GaSb/AlSb systems, *Appl. Phys. Lett.* **70**, 481 (1997).
- [19] J. Li, K. Chang, G. Q. Hai, and K. S. Chan, Anomalous Rashba spin-orbit interaction in InAs/GaSb quantum wells, *Appl. Phys. Lett.* **92**, 152107 (2008).
- [20] F. Qu, A. J. A. Beukman, S. Nadj-Perge, M. Wimmer, B.-M. Nguyen, W. Yi, J. Thorp, M. Sokolich, A. A. Kiselev, M. J. Manfra, C. M. Marcus, and L. P. Kouwenhoven, Electric and Magnetic Tuning Between the Trivial and Topological Phases in InAs/GaSb Double Quantum Wells, *Phys. Rev. Lett.* **115**, 036803 (2015).
- [21] K. Suzuki, Y. Harada, K. Onomitsu, and K. Muraki, Gate-controlled semimetal-topological insulator transition in an InAs/GaSb heterostructure, *Phys. Rev. B* **91**, 245309 (2015).
- [22] N. Dagli, Wide-bandwidth lasers and modulators for RF photonics, *IEEE Trans. Microwave Theory Tech.* **47**, 1151 (1999).
- [23] G. Li and P. Yu, Optical intensity modulators for digital and analog applications, *J. Lightwave Technol.* **21**, 2010 (2003).
- [24] J. Li and K. Chang, Electric field driven quantum phase transition between band insulator and topological insulator, *Appl. Phys. Lett.* **95**, 222110 (2009).
- [25] J. Li, W. Yang, J.-T. Liu, W. Huang, C. Li, and S.-Y. Chen, Enhanced circular photogalvanic effect in HgTe quantum wells in the heavily inverted regime, *Phys. Rev. B* **95**, 035308 (2017).
- [26] R. W. Boyd, in *Nonlinear Optics (Third Edition)*, edited by R. W. Boyd (Academic Press, Burlington, 2008) third edition ed., p. 135.
- [27] M. Helm, *Intersubband Transitions in Quantum Wells: Physics and Device Applications I*, edited by H. Liu and F. Capasso, Semiconductors and Semimetals, Vol. 62 (Elsevier, 1999), p. 1.
- [28] R. J. Warburton, C. Gauer, A. Wixforth, J. P. Kotthaus, B. Brar, and H. Kroemer, Intersubband resonances in InAs/AlSb quantum wells: Selection rules, matrix elements, and the depolarization field, *Phys. Rev. B* **53**, 7903 (1996).
- [29] M. F. Pereira, S.-C. Lee, and A. Wacker, Controlling many-body effects in the midinfrared gain and terahertz absorption of quantum cascade laser structures, *Phys. Rev. B* **69**, 205310 (2004).
- [30] J. Li and C. Z. Ning, Interplay of Collective Excitations in Quantum-Well Intersubband Resonances, *Phys. Rev. Lett.* **91**, 097401 (2003).
- [31] Q. Hao, G. Zhu, S. Yang, K. Yang, T. Duan, X. Xie, K. Huang, and H. Zeng, Mid-infrared transmitter and receiver modules for free-space optical communication, *Appl. Opt.* **56**, 2260 (2017).
- [32] A. Delga and L. Leviandier, in *Quantum Sensing and Nano Electronics and Photonics XVI*, Vol. 1092617, edited by M. Razeghi, J. S. Lewis, G. A. Khodaparast, and E. Tournié (SPIE, 2019), p. 40.
- [33] J. J. Liu, B. L. Stann, K. K. Klett, P. S. Cho, and P. M. Pellegrino, in *Laser Communication and Propagation through the Atmosphere and Oceans VIII*, Vol. 1113302, edited by A. M. van Eijk, S. Hammel, and J. P. Bos (SPIE, 2019), p. 1.
- [34] X. Pang, O. Ozolins, L. Zhang, R. Schatz, A. Udalcovs, X. Yu, G. Jacobsen, S. Popov, J. Chen, and S. Lourduodoss, Free-space communications enabled by quantum cascade lasers, *Phys. Status Solidi (a)* **218**, 2000407 (2021).
- [35] J. Mikołajczyk, Data link with a high-power pulsed quantum cascade laser operating at the wavelength of 4.5 μm , *Sensors* **21**, 3231 (2021).
- [36] O. Spitz, P. Didier, L. Durupt, D. A. Diaz-Thomas, A. N. Baranov, L. Cerutti, and F. Grillot, Free-space communication with directly modulated mid-infrared quantum cascade devices, *IEEE J. Sel. Top. Quantum Electron.* **28**, 1 (2022).
- [37] F. Capasso, R. Paiella, R. Martini, R. Colombelli, C. Gmachl, T. L. Myers, M. S. Taubman, R. M. Williams, C. G. Bethea, and K. Unterrainer, *et al.*, Quantum cascade lasers: Ultrahigh-speed operation, optical wireless communication, narrow linewidth, and far-infrared emission, *IEEE J. Quantum Electron.* **38**, 511 (2002).
- [38] B. Hinkov, A. Hugi, M. Beck, and J. Faist, Rf-modulation of mid-infrared distributed feedback quantum cascade lasers, *Opt. Express* **24**, 3294 (2016).
- [39] A. Mottaghizadeh, Z. Asghari, M. Amanti, D. Gacemi, A. Vasanelli, and C. Sirtori, in *2017 42nd International Conference on Infrared, Millimeter, and Terahertz Waves (IRMMW-THz)* (IEEE, 2017), p. 1.
- [40] S. Pirota, N.-L. Tran, A. Jollivet, G. Biasiol, P. Crozat, J.-M. Manceau, A. Bousseksou, and R. Colombelli, Fast amplitude modulation up to 1.5 GHz of mid-IR free-space beams at room-temperature, *Nat. Commun.* **12**, 799 (2021).
- [41] N. Vodjdani, B. Vinter, V. Berger, E. Böckenhoff, and E. Costard, Tunneling assisted modulation of the intersubband absorption in double quantum wells, *Appl. Phys. Lett.* **59**, 555 (1991).
- [42] E. Dupont, D. Delacourt, V. Berger, N. Vodjdani, and M. Papuchon, Phase and amplitude modulation based on intersubband transitions in electron transfer double quantum wells, *Appl. Phys. Lett.* **62**, 1907 (1993).
- [43] J. Y. Duboz, V. Berger, N. Laurent, D. Adam, and J. Nagle, Grating coupled infrared modulator at normal incidence based on intersubband transitions, *Appl. Phys. Lett.* **70**, 1569 (1997).
- [44] Y. C. Jun, E. Gonzales, J. L. Reno, E. A. Shaner, A. Gabbay, and I. Brener, Active tuning of mid-infrared metamaterials by electrical control of carrier densities, *Opt. Express* **20**, 1903 (2012).
- [45] Z. Li and N. Yu, Modulation of mid-infrared light using graphene-metal plasmonic antennas, *Appl. Phys. Lett.* **102**, 131108 (2013).

- [46] J. Chiles and S. Fathpour, Mid-infrared integrated waveguide modulators based on silicon-on-lithium-niobate photonics, *Optica* **1**, 350 (2014).
- [47] R. Q. Yang, L. Li, W. Huang, S. M. S. Rassel, J. A. Gupta, A. Bezinger, X. Wu, S. G. Razavipour, and G. C. Aers, InAs-based interband cascade lasers, *IEEE J. Sel. Top. Quantum Electron.* **25**, 1 (2019).
- [48] Since the p -doped layer might cause excessive absorption loss, one could also consider employing an n^+ -doped InAs/AlSb SL as the upper cladding layer to lower the total insertion loss of the EAM, as long as the external applied voltage is able to induce sufficient absorption modulation and the leakage current can be controlled.
- [49] E. H. Edwards, R. M. Audet, E. T. Fei, S. A. Claussen, R. K. Schaevitz, E. Tasyurek, Y. Rong, T. I. Kamins, J. S. Harris, and D. A. B. Miller, Ge/SiGe asymmetric fabry-perot quantum well electroabsorption modulators, *Opt. Express* **20**, 29164 (2012).
- [50] W. W. Bewley, C. L. Canedy, C. S. Kim, C. D. Merritt, M. V. Warren, I. Vurgaftman, J. R. Meyer, and M. Kim, Room-temperature mid-infrared interband cascade vertical-cavity surface-emitting lasers, *Appl. Phys. Lett.* **109**, 151108 (2016).
- [51] R. Colombelli, K. Srinivasan, M. Troccoli, O. Painter, C. F. Gmachl, D. M. Tennant, a. M. Sergent, D. L. Sivco, A. Y. Cho, and F. Capasso, Quantum cascade surface-emitting photonic crystal laser, *Science* **302**, 1374 (2003).
- [52] L. Marigo-Lombart, S. Calvez, A. Arnoult, H. Thienpont, G. Almuneau, and K. Panajotov, Vertical electro-absorption modulator design and its integration in a VCSEL, *J. Phys. D: Appl. Phys.* **51**, 145101 (2018).
- [53] L. Marigo-Lombart, S. Calvez, A. Arnoult, A. Rumeau, C. Viallon, H. Thienpont, K. Panajotov, and G. Almuneau, in *Vertical-Cavity Surface-Emitting Lasers XXII*, February 2018, edited by K. D. Choquette and C. Lei (SPIE, 2018), p. 20.
- [54] M. Chin and W. Chang, Theoretical design optimization of multiple-quantum-well electroabsorption waveguide modulators, *IEEE J. Quantum Electron.* **29**, 2476 (1993).
- [55] R. Weinmann, U. Cebulla, J. Weber, D. Baums, E. Kühn, K. Satzke, E. Zielinski, P. Wiedemann, E. Lach, D. Kaiser, and H. Haisch, Ultrahigh-bandwidth (42 GHz) polarisation-independent ridge waveguide electroabsorption modulator based on tensile strained InGaAsP MQW, *Electron. Lett.* **31**, 2030 (1995).
- [56] F. Devaux, S. Chelles, A. Ougazzaden, A. Mircea, and J. C. Harmand, Electroabsorption modulators for high-bit-rate optical communications: A comparison of strained InGaAs/InAlAs and InGaAsP/InGaAsP MQW, *Semicond. Sci. Technol.* **10**, 887 (1995).
- [57] M. Pamplona Pires, P. Lustoza de Souza, B. Yavich, R. Pereira, and W. Carvalho, On the optimization of InGaAs-InAlAs quantum-well structures for electroabsorption modulators, *J. Lightwave Technol.* **18**, 598 (2000).
- [58] M. Chin, Comparative analysis of the performance limits of Franz-Keldysh effect and quantum-confined Stark effect electroabsorption waveguide modulators, *IEE Proceedings - Optoelectronics* **142**, 109 (1995).
- [59] I. Knez, R. R. Du, and G. Sullivan, Finite conductivity in mesoscopic Hall bars of inverted InAs/GaSb quantum wells, *Phys. Rev. B* **81**, 201301(R) (2010).
- [60] T. Akiho, F. Couëdo, H. Irie, K. Suzuki, K. Onomitsu, and K. Muraki, Engineering quantum spin Hall insulators by strained-layer heterostructures, *Appl. Phys. Lett.* **109**, 192105 (2016).
- [61] L. Du, T. Li, W. Lou, X. Wu, X. Liu, Z. Han, C. Zhang, G. Sullivan, A. Ikhlassi, K. Chang, and R.-r. Du, Tuning Edge States in Strained-Layer InAs/GaInSb Quantum Spin Hall Insulators, *Phys. Rev. Lett.* **119**, 056803 (2017).
- [62] A. Spott, E. J. Stanton, A. Torres, M. L. Davenport, C. L. Canedy, I. Vurgaftman, M. Kim, C. S. Kim, C. D. Merritt, and W. W. Bewley, *et al.*, Interband cascade laser on silicon, *Optica* **5**, 996 (2018).
- [63] J. R. Meyer, C. S. Kim, M. Kim, C. L. Canedy, C. D. Merritt, W. W. Bewley, and I. Vurgaftman, Interband cascade photonic integrated circuits on native III-V chip, *Sensors* **21**, 599 (2021).
- [64] T. Ando, A. B. Fowler, and F. Stern, Electronic properties of two-dimensional systems, *Rev. Mod. Phys.* **54**, 437 (1982).
- [65] S. Allen, D. Tsui, and B. Vinter, On the absorption of infrared radiation by electrons in semiconductor inversion layers, *Solid State Commun.* **20**, 425 (1976).
- [66] T. Ando, Inter-subband optical transitions in a surface space-charge layer, *Solid State Commun.* **21**, 133 (1977).